

# Forecasting Melting Points in Svalbard, Norway Using Quantile Gradient Boosting and Adaptive Conformal Prediction Regions

Richard Berk

*University of Pennsylvania*

*Corresponding author: berkr@sas.upenn.edu*

*ORCID: <https://orcid.org/0000-0002-2983-1276>*

**Abstract:** Using data from the Longyearbyen weather station, quantile gradient boosting (“small AI”) is applied to forecast daily 2023 temperatures in Svalbard, Norway. The 0.60 quantile loss weights underestimates about 1.5 times more than overestimates. Predictors include five routinely collected indicators of weather conditions, each lagged by 14 days, yielding temperature forecasts with a two-week lead time. Conformal prediction regions quantify forecasting uncertainty with provably valid coverage. Forecast accuracy is evaluated with attention to local stakeholder concerns, and implications for Arctic adaptation policy are discussed.

**Keywords and phrases:** Arctic melting, forecasting, quantile gradient boosting, quantile regression forests, conformal prediction regions.

## 1. Introduction

The oceans and cryosphere interact to support unique ecosystems while exchanging water, energy, and carbon with Earth’s climate system. The 2019 *Intergovernmental Panel on Climate Change* (IPCC) report concludes that global warming has altered this interaction, causing “mass loss from ice sheets and glaciers, reductions in snow cover, decreases in Arctic sea-ice extent and thickness, and increased permafrost temperatures” (IPCC, 2019, A.1). Ecosystem impacts have been equally dramatic (IPCC, 2019, A.4).

A key feature of the IPCC report is its reliance on forecasts at very large spatial and temporal scales, consistent with planet-wide coverage and the gradual pace of climate change. Spatial scales can span thousands of square

kilometers.<sup>1</sup> Projections typically extend years into the future.

The goals of numerical weather prediction (NWP) differ from those of climate modeling and require much finer spatial and temporal detail.<sup>2</sup> Although NWP calculations are performed at much smaller scales, the resulting forecasts still aggregate across those spatial and temporal units. Forecasts for specific sites represent averages across larger areas, and hourly predictions are aggregates over seconds and minutes.

The coarse spatial and temporal resolution characterizing GCMs and NWP is especially consequential for forecasts in high-latitude regions such as the Arctic, where small temperature differences around the local freezing point can have major implications for phenomena such as “Arctic amplification,” discussed in more detail below. This motivates the development of complementary forecasting approaches that can resolve finer spatial and temporal detail, particularly when informing short-term adaptation measures in specific locales.

There are further difficulties. The conditions forecast are usually standardized. The snowfall expected in, say, Fairbanks, Alaska, “during the next 24 hours” is an example. Different locations, however, may wish to supplement such forecasts. In the Arctic, local officials might want to know well in advance the probability that 0°C will be exceeded. Such information could guide the timing of sediment removal, pre-emptive slope closures, and preparation of

---

<sup>1</sup>For example, the *Community Earth System Model* version 2 (CESM2) is typically run at nominal 1° resolution, corresponding to grid cells of roughly 10,000–15,000 km<sup>2</sup>, depending on latitude. Downscaling methods have been proposed for regional grids, but they rest on strong assumptions about the parent Global Climate Model (GCM), and no consensus has emerged on a preferred approach (Nishizawa et al., 2018). Moreover, finer spatial grids would greatly increase computational demands that are already near prohibitive. The temporal scale reflects grid cells updated internally every 30 minutes, with atmosphere–land–ocean–ice coupling on hourly intervals and outputs usually produced as daily or monthly means (Danabasoglu et al., 2020; National Center for Atmospheric Research, 2020).

<sup>2</sup>Global weather prediction systems, such as ECMWF’s Integrated Forecasting System (IFS) and NOAA’s Global Forecast System (GFS), use grid cells covering on the order of 80–200 km<sup>2</sup>. Even the most advanced regional models, such as NOAA’s High-Resolution Rapid Refresh (HRRR) or the Weather Research and Forecasting (WRF) model, employ grid spacings of 1–3 km and still aggregate conditions across areas of 1–9 km<sup>2</sup>. Their time steps are on the order of seconds to minutes, with outputs every 1–3 hours for global models and hourly (or finer) for regional models (European Centre for Medium-Range Weather Forecasts, 2023; NOAA National Centers for Environmental Prediction, 2023; NOAA Earth System Research Laboratory, 2023).

wastewater systems for meltwater discharge, among other actions.

Estimating forecast uncertainty remains problematic (Fu, 2025). Gentleman and Rood (2016, 12) summarize the challenges for climate models, which apply equally to weather forecasting: “Uncertainty in climate models has several components. They are related to the model itself, to the initial conditions of the model, and to the inputs that affect the model. All three must be addressed for the model to be useful.”

There have been recent technical advances, to be sure (Pathak et al., 2022; Price et al., 2024; Bodnar et al., 2025). Yet issues of coarse spatial scales, standardized output, and uncertain reliability remain largely unresolved (Ortega et al., 2022; Balaji et al., 2022; Chang et al., 2023). This paper uses Svalbard, Norway, as a test case to advance Arctic temperature forecasting while addressing these three limitations. Temperatures are the focus because of growing global concern over rising heat.

Section 2 provides background on Svalbard and the forecasting challenges posed by Arctic amplification. Section 3 describes the data, the construction of holdout samples, and the 14-day lagging of predictors used to support legitimate forecasting. Section 4 introduces the statistical methods, focusing on quantile supervised learning. Section 5 presents the empirical results, emphasizing visualization and model interpretation. Section 6 addresses uncertainty through conformal prediction regions for multiple time-series data and offers a grounded way to communicate forecast reliability to stakeholders. Section 7 discusses policy implications, with emphasis on short-fuse adaptations to Arctic melting, and Section 8 concludes. Pseudocode for the conformal inference procedure appears in the Appendix.

## 2. Svalbard, Norway: The Forecasting Setting

Svalbard is a remote Norwegian archipelago in the Arctic Ocean, located about halfway between mainland Norway and the North Pole. Its main settlement, Longyearbyen, lies at roughly 78°N latitude, well above the Arctic Circle. Only a small fraction of the land is vegetated, mostly tundra, while the remainder is dominated by permafrost, ice, and bare rock. Longyearbyen is one of the northernmost permanently inhabited places on Earth.

The maritime climate is distinctive in part because Svalbard is warmed by Atlantic Ocean currents. Average winter temperatures in Longyearbyen range from about  $-20^{\circ}\text{C}$  to  $-14^{\circ}\text{C}$ , while summers are cool, typically between  $3^{\circ}\text{C}$

and 7°C. In recent years, temperatures have more often spiked above 10°C, a trend climate scientists find troubling.

Snow falls during much of the year, but total precipitation is relatively low, technically making Svalbard a polar desert. From late October to mid-February the archipelago experiences the polar night, when the sun does not rise above the horizon. From mid-April to late August the sun remains above the horizon, bringing continuous daylight. In recent decades Svalbard has warmed at a rate several times the global average, with mean winter temperatures increasing by more than 5°C since the 1970s. Glaciers are retreating, sea ice is thinning, and thawing permafrost is reshaping the terrain. The archipelago is now among the world's most affected regions of climate change (Urbański and Litwicka, 2022; Karlsen et al., 2024; Bradley et al., 2025; Schuler et al., 2025).

### ***2.1. Some Implications for Forecasting Temperatures***

A practical attraction of Svalbard for temperature forecasting is the weather station at Longyearbyen Airport, whose data are curated by NOAA in collaboration with its international partners. These data are freely available and easy to download. Under the Svalbard Treaty of 1920, Norway retains sovereignty but grants citizens of other signatory nations equal rights to engage in scientific and commercial activities. Several international research stations are operated by Russia, Poland, Germany, China, the United States, and others.

A scientific attraction is that Svalbard's maritime climate presents a demanding test for Arctic temperature forecasting. Unlike continental climates at comparable latitudes, one cannot simply look westward and project that those temperatures will arrive several days later. Immediately to the west lies the Arctic Ocean, not a large landmass with comparable terrain.

Another forecasting challenge is the especially rapid climatic change occurring throughout polar regions such as Svalbard, often termed "Arctic amplification" (Rantanen et al., 2022). The farther one moves from the equator, the faster the rate of warming. Early explanations emphasized the declining albedo caused by sea-ice loss and the increasing exposure of tundra and rock. As more sunlight is absorbed and less reflected, additional heat is retained, reinforcing local warming through a strong positive feedback loop.

Semenov (2021) notes that at least two additional mechanisms are now recognized as important contributors to Arctic amplification. Their most

fundamental feature is the *Planck effect*. In simple terms, the Planck effect describes how efficiently Earth radiates heat into space. That efficiency—the rate at which the outgoing energy flux increases with temperature—is smaller in colder regions. Because the radiative flux follows the Stefan–Boltzmann law, its slope with respect to temperature ( $T$ ) is proportional to  $T^3$ . At the low surface temperatures typical of the polar regions, this slope is relatively flat. As a result, the polar surface radiates infrared energy less effectively than warmer regions experiencing the same temperature increase; heat therefore accumulates more rapidly.

The same Planck effect also operates higher in the atmosphere. The “effective emission height” is the average altitude from which the planet’s infrared radiation escapes directly to space. As greenhouse-gas concentrations rise, this emission level shifts upward. Because temperature generally decreases with altitude, radiation then originates from colder air. By the same  $T^3$  relationship, the efficiency of infrared emission is reduced. Thus, the Planck effect contributes to polar amplification in two ways: directly at the cold surface and indirectly aloft through the upward shift of the emission height to colder temperatures. Arctic amplification provides an essential context for the forecasting that follows.

### 3. Data

The data come from the Longyearbyen weather station. Observations for 2023 are used for training. Data from 2022 provide “honest” assessments of the number of algorithm iterations required, and the 2024 data serve as a fully pristine holdout sample used as “new cases” to document true forecasting skill. They play no role in training. The assumptions required to combine all three datasets are discussed shortly. Data from 2021 are also used for variable construction, as described below.

The downloaded data provide hourly observations within each day. Hourly data are too detailed for the analyses to follow and add unnecessary complexity; daily data are used instead. The response variable is the daily solar-time 2 p.m. air temperature in degrees Celsius at the Longyearbyen weather station. Daily temperature values at 2 p.m. solar time are taken from the Integrated Surface Database using the *worldmet* package in R. 2 p.m. value is an *instantaneous observation*—a snapshot of conditions at a constant daily reference time rather than an hourly or daily mean. The 2 p.m. solar-time convention is used uniformly throughout the year, including during the polar night, to provide a

consistent temporal reference for forecasting. This differs from global climate and numerical weather prediction procedures, which typically rely on spatially and temporally averaged fields.

Predictors are all *lagged by 14 days*. They include (1) wind direction in degrees from true north, (2) wind speed in meters per second, (3) air temperature in degrees Celsius, (4) atmospheric pressure in hectopascals (hPa), (5) visibility in meters, (6) dew point in degrees Celsius, (7) relative humidity in percent, and (8) a day counter ranging from 1 to 365. The counter can capture temporal trends: on average, the diurnal months are warmer than the nocturnal months, although temperature changes over time may be nonlinear. Several predictors are likely to interact in complex ways (Semenov, 2021). The 14-day lags translate into fitted 2 p.m. temperatures two weeks later, yielding forecasts two weeks in advance.<sup>3</sup>

The complete dataset forms a multiple time series, making temporal dependence a potential complication. Holdout samples drawn at random from the 2023 training data would obscure any such dependence (Hyndman and Athanasopoulos, 2021, sec. 5.8). Instead, separate holdouts from 2022 and 2024 are used. The same physical processes should apply during the identical months of 2022, 2023, and 2024; data for all three years are treated as random realizations from the same underlying joint probability distribution. Nonetheless, Arctic amplification may affect this comparability, an issue examined empirically in Section 5.2.

## 4. Statistical Methods

### 4.1. *Background*

Models and algorithms from statistics and computer science are increasingly used in climate and weather applications (Ma et al., 2023; Miloshevich et al., 2024; Kvånum et al., 2025). Especially relevant to the analyses that follow is the work of Velthoen et al. (2023), who analyzed several years of daily precipitation observations from the Dutch KNMI weather-station network. The precipitation distribution exhibits a long right tail. Weather-station data provide one source of predictors; deterministic precipitation forecasts from

---

<sup>3</sup>Lagging variables is a routine procedure in feature construction. In this case, however, lagging the first 14 days of a year pushes their reference points into the final 14 days of the previous year. Data from 2021 are therefore included to provide lagged values for the first 14 days of 2022. Otherwise, the 2021 data are not used.

the ECMWF weather model provide another. Combined, these data form a multiple time series.

The authors developed *gbex*, a quantile gradient-boosting algorithm (Friedman, 2001, 2002) tailored to rare and extreme precipitation events using conditional quantiles at very high levels (e.g., 0.95 or 0.99). Quantile regression methods typically struggle when either tail is sparse. The *gbex* procedure borrows strength from Extreme-Value Theory (EVT) by fitting a Generalized Pareto Distribution (GPD) to values exceeding a high threshold while allowing the GPD parameters to depend on predictors via quantile gradient boosting. The approach was “validated” by comparing the *gbex* results with classical methods such as quantile linear regression (Koenker, 2005), showing superior calibration for the extremes.

There is much to admire in Velthoen et al. (2023), but the analyses that follow depart in several important respects. The setting is above the Arctic Circle, where climate and weather processes differ substantially. Consequently, extreme events are not the primary focus; quantile gradient boosting is employed for other purposes.

No enhancements from parametric statistical procedures are used. As Breiman (2001) emphasized, there is considerable skepticism toward statistical modeling unless it has been thoroughly vetted. Nor is algorithmic tuning employed, to avoid post-model-selection bias (Kuchibhotla, Kolassa and Kuffner, 2022). The goal is to perform genuine forecasting, evaluated with independent holdout samples.

Time-series data often exhibit substantial temporal dependence. To obtain valid assessments of forecasting accuracy and uncertainty, the training procedure is expanded to account for this dependence. The analyses adopt standard time-series methods (Box et al., 2015) as a training enhancement.

Finally, provably valid estimates of forecasting uncertainty are obtained using adaptive conformal prediction regions (Romano, Patterson and Candès, 2019). The requisite exchangeability is addressed explicitly, and supplemental results are provided that may be of particular interest to stakeholders.

#### **4.2. The Statistical Procedures Used**

The Arctic multiple time-series data described above are analyzed using quantile gradient boosting, with the 60th percentile (i.e.,  $Q(0.60)$ ) as the estimation target. Let  $y$  denote the numeric response variable,  $\hat{y}$  its fitted value,

and  $\tau$  the target conditional quantile. Quantile gradient boosting minimizes the following loss function (Koenker and Bassett Jr, 1978):

$$L_\tau(y, \hat{y}) = \begin{cases} \tau \cdot (y - \hat{y}), & \text{if } y \geq \hat{y}, \\ (1 - \tau) \cdot (\hat{y} - y), & \text{if } y < \hat{y}. \end{cases} \quad (1)$$

With  $\tau = 0.60$ , underestimates receive  $0.6/0.4 = 1.5$  times more weight than overestimates when loss is computed. For this application, about 40% of the 2023 Longyearbyen temperatures exceed  $0^\circ\text{C}$ . Because relatively high values tend to be underestimated and relatively low values overestimated, fitting the conditional 0.60 quantile forces the gradient-boosting algorithm to work harder to avoid underestimates. This occurs most often among the warmest 40% of temperatures. Indirectly, therefore, these “melting days” are weighted more heavily than the rest. Melting days are of particular concern under Arctic amplification, often requiring practical climate adaptations.

If melting days are so important, one might argue for reformulating the analysis as a classification problem—above or below  $0^\circ\text{C}$ . While melting is indeed a critical threshold, the degree to which that threshold is exceeded also matters. The melting process is highly nonlinear and difficult to characterize, but evidence suggests that melting increases at an increasing rate as temperatures rise (Polashenski, Perovich and Courville, 2012; Pizner et al., 2024).

Adaptive conformal prediction regions provide provably valid coverage when data are exchangeable. Multiple time-series data, however, are typically not exchangeable. With an appropriate fitting algorithm, this limitation can be addressed. Details and supporting pseudocode are presented later, in the grounded context of the forecasting results. The approach is at least unusual, and perhaps even novel.

## 5. Results

The results begin with simple univariate plots to provide context for the more involved analyses. Because of the months-long alternation between daylight and darkness, Arctic temperatures fluctuate differently from those at lower latitudes. In general, the figures that follow should be largely self-explanatory.

### 5.1. Univariate Plots

As a sanity check, a time series of the 2 p.m. temperatures for 2023 should reflect the expected Arctic seasonal swings. Figure 1 (left panel) shows precisely that. The light-blue irregular line interpolates the daily temperatures, while the smooth black line represents a loess smoother applied to those values. The red horizontal line marks the melting point at 0°C. Temperatures during the nocturnal months are, on average, colder than during the diurnal months, and transitions between them are gradual. Melting temperatures are common from early June through late September.

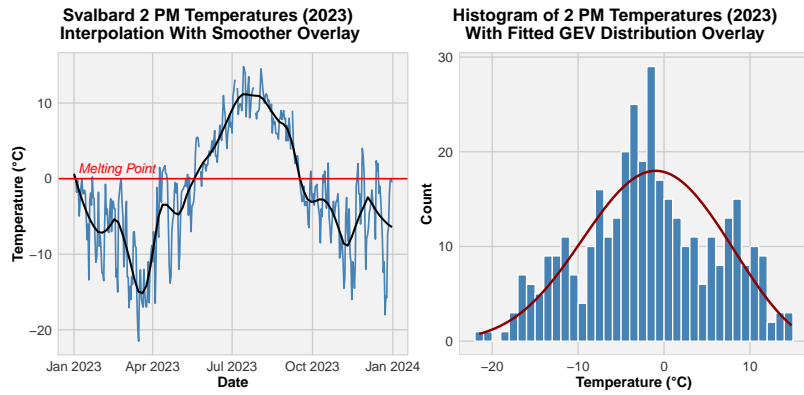


FIG 1. 2 p.m. 2023 temperatures with the time-series plot in the left panel and the histogram with a GEV distribution overlay in the right panel.

The right panel shows a histogram of the 2 p.m. temperatures for 2023 with a generalized extreme value (GEV) distribution overlay. Temperatures range from slightly below  $-20^{\circ}\text{C}$  to slightly above  $10^{\circ}\text{C}$ , revealing substantial variability to study. The GEV overlay adds little interpretive value. The histogram is roughly symmetric, although the left tail is somewhat longer than the right. No clear outliers are apparent.

### 5.2. Time-Series Plot for Svalbard Temperatures in 2022, 2023, and 2024

Recall the premise that each time series of daily 2 p.m. temperatures for 2022, 2023, and 2024 ideally represents realizations from the same underlying joint probability distribution—the underlying physics for corresponding months in

those three years should be comparable. However, concerns have been raised about possible departures due to Arctic amplification.

Figure 2 provides a visual comparison of the three temperature time series. The jagged lines show the 2 p.m. daily temperatures plotted against day of year, and the dashed horizontal line marks the melting temperature at 0°C.

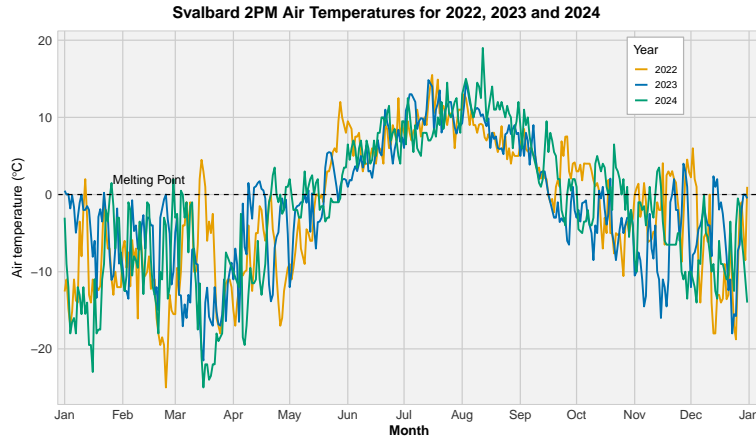


FIG 2. Daily 2 p.m. temperatures for 2022, 2023, and 2024 using a color palette that is color-blind friendly.

Figure 2 shows substantial overlap among the three years. Seasonal trends are captured in a similar manner, both in temperature levels and in timing. The time series move largely in lockstep from early to late summer, when melting temperatures are nearly universal. There appears to be no compelling reason to reject the claim that each series consists of random variables drawn from the same joint probability distribution. In practice, the 2022 and 2024 temperatures serve as promising holdout-sample candidates for evaluating forecasts of the 2023 temperatures.

### 5.3. The Quantile GBM Fit of Temperature

With the quantile parameter fixed at  $\tau = 0.60$ , the quantile gradient-boosting procedure in R ran efficiently. The shrinkage value was set to 0.0001, the interaction depth to 6, and the minimum number of observations in a terminal node to 6. These values were chosen to foster slow convergence so that the tails of the temperature distribution would be fitted more accurately. Using

2022 as a holdout sample indicated that approximately 27,000 iterations were appropriate for these data.<sup>4</sup>

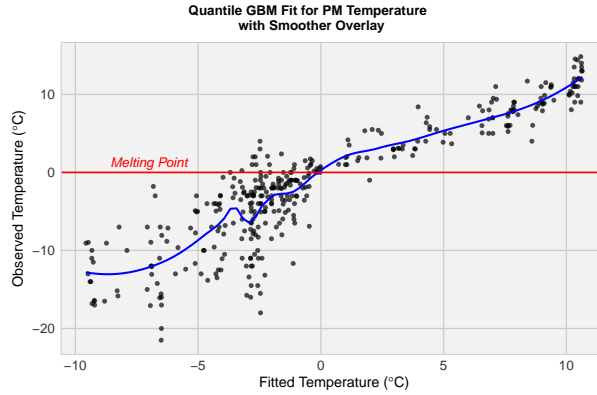


FIG 3. Observed versus fitted 2 p.m. temperatures. Black dots are the data, the blue solid line is a loess smooth, and the red horizontal line marks the melting point at 0°C.

Figure 3 plots the observed 2 p.m. temperatures against their fitted values. The relationship is roughly linear and positive: observed and fitted values tend to increase together. The clustering around the smoothed fitted line is somewhat tighter when the fitted values exceed the melting point, with residuals rarely larger than about  $\pm 2^\circ\text{C}$ . This results in part from the heavier weighting of those values through the target quantile  $\tau = 0.60$ . There is greater sparsity on either side of the temperature range between approximately  $-5^\circ\text{C}$  and  $0^\circ\text{C}$ .

Koenker and Machado (1999) discuss measures of fit for conditional-quantile models derived from the quantile loss function. However, no analogue of the multiple correlation coefficient exists for quantile regression. A suitable measure of fit is introduced later, when conformal prediction regions are presented.

Two points merit emphasis. First, the apparent linearity in Figure 3 says nothing about whether the lagged predictors themselves relate linearly to temperature. In Figure 1, the  $x$ -axis units are days; in Figure 3, they are

<sup>4</sup>With a substantially larger shrinkage value, many fewer iterations might have been adequate. However, the best shrinkage value could not be known in advance, and selectively tuning parameters can undermine later statistical inference (Kuchibhotla, Kolassa and Kuffner, 2022).

degrees Celsius. The former shows day-to-day variation in observed temperatures, whereas the latter shows how observed temperatures vary with their fitted counterparts. Second, lagging the predictors means they generate fitted values *two weeks before* the future temperatures materialize. This is not true forecasting, since no new unlabeled cases are involved, but it is an important step in that direction.<sup>5</sup>

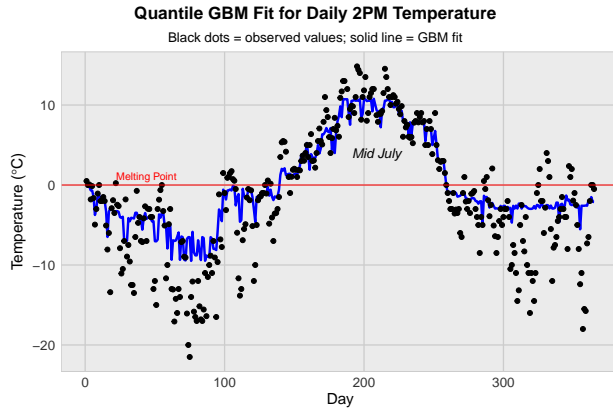


FIG 4. Observed daily 2 p.m. temperatures and fitted values from quantile gradient boosting plotted against day of year (2023). The solid red line marks the melting point at 0°C.

Figure 4 provides a complementary perspective that connects more directly to the Arctic-amplification context. It re-expresses the results from Figure 3 as a time series, plotting temperature against day of year. As before, black dots denote the observed 2 p.m. temperatures, the jagged blue line shows the fitted values from quantile gradient boosting, and the horizontal red line marks the melting point.

Overall, the fitted values track the observed temperatures closely and capture temperatures above 0°C especially well. The several unusually warm days clustering in mid-July—around 10°C—are of particular concern to climate scientists (Semenov, 2021), and they too are fitted accurately, albeit with slight underestimation. Two weeks in advance, the fitted algorithm anticipates melting temperatures effectively, including those mid-July extremes. The fit might improve further if a larger value of  $\tau$  were used, but higher quantiles

<sup>5</sup>Fitted values are sometimes called predicted values, which can cause confusion. In this paper, the term *fitted values* refers to outcomes within the training data, whereas *forecasted values* refer to predictions for new, unseen cases.

(e.g.,  $Q(0.90)$ ) would rely on far sparser data, potentially leading to instability. As with Figure 3, however, true forecasting still remains to be performed.

#### 5.4. Predictor Impacts on the Fitted Values

Like all algorithms, quantile gradient boosting is not a model in the traditional statistical sense (Breiman, 2001; Kearns and Roth, 2019). Nevertheless, useful insights about associations among variables can be obtained from variable-importance plots and partial-dependence plots (Friedman, 2002).

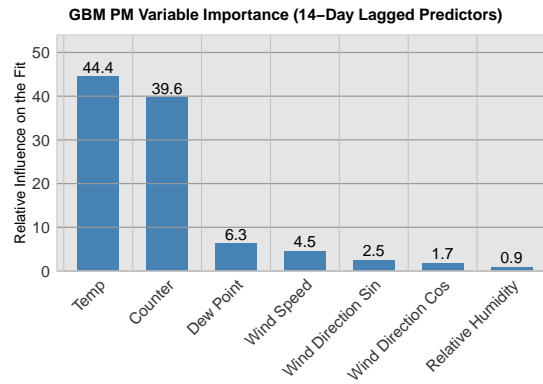


FIG 5. *Relative contribution of each lagged predictor to the fitted 2 p.m. temperatures, computed as the standardized reduction in loss attributable to each predictor.*

From the variable-importance plot in Figure 5, the day counter and the 2 p.m. temperature lagged by 14 days have by far the strongest associations with the fit of subsequent 2 p.m. temperatures. Rounding slightly, the former accounts for about 40% of the total reduction in loss, and the latter for a bit more than 45%. The remaining lagged predictors together contribute a little over 10%. The sum of all contributions is approximately 100%.

The prominence of the day counter and the 14-day temperature lag is unsurprising. Clear seasonal patterns are captured by the counter, and temperature's gradual evolution over time makes its own lag a strong predictor. The other variables may still capture small or localized temporal effects that, while contributing less to predictive accuracy, could be of scientific or policy interest.

### 5.5. Functional Forms

The quantile gradient-boosting algorithm learns associations between each predictor and the response, including the shapes of those relationships. The partial-dependence plots in Figure 6 show the relationships between the day counter and the 14-day lagged temperature with the temperature response variable, each computed with all other predictors fixed at their means—that is, all other predictors are “held constant.” These are the two variables that dominate the fit. The black dots represent the partial-dependence values, and the solid blue lines show a loess smooth of those values.

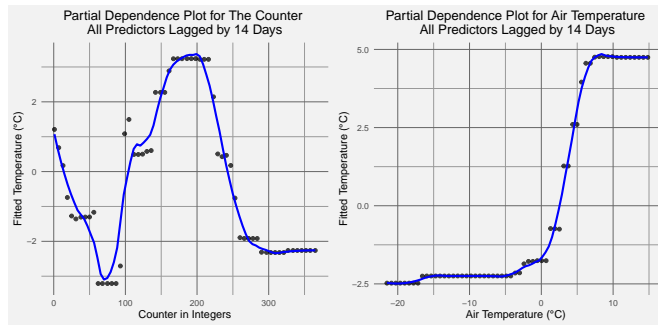


FIG 6. Partial-dependence plots for the day counter and 14-day lagged temperature. The black dots are the partial-dependence values, and the solid blue line is a loess smooth. Both panels show the relationship with the response variable while all other predictors are fixed at their means.

Consistent with Figure 5, strong relationships are evident. The counter-based fitted values range from approximately  $-3^{\circ}\text{C}$  to  $3^{\circ}\text{C}$ , and the lagged-temperature fitted values from about  $-2.5^{\circ}\text{C}$  to  $5^{\circ}\text{C}$ . The first plot is roughly symmetric and concave, peaking during the summer months, consistent with the longitudinal pattern shown in Figure 4. The second plot is S-shaped, with its steepest slope beginning immediately after the melting point at  $0^{\circ}\text{C}$  is reached and plateauing near  $-2.5^{\circ}\text{C}$  and  $5^{\circ}\text{C}$ . The lagged observed temperatures have their strongest association with fitted temperatures just above the melting point. The practical significance of this threshold will be discussed in greater depth below.<sup>6</sup>

<sup>6</sup>The short strings of dots visible in the plot represent rounding artifacts; the values differ slightly.

The remaining four predictors also exhibit nonlinear relationships with the temperature response variable, but because of their comparatively small contributions to the fit, their partial-dependence plots are omitted here in the interest of space.

## 6. Forecasts and Estimated Uncertainty

Conformal prediction regions begin with a pre-specified coverage probability. By convention, this probability is denoted  $(1 - \alpha)$ , where  $\alpha$  lies between 0 and 0.50. In practice, coverage probabilities range from slightly above 0.50 to nearly 1.0, with values between 0.75 and 0.99 most common. The value of  $\alpha$  is determined by subjective considerations shaped by the data and the application.

Once a coverage probability is specified, the data are used to determine the length of each prediction region. A conformal prediction region contains the true forecasted value with probability at least  $(1 - \alpha)$ , conditional on the training data and the performance of the fitted algorithm (Vovk, Gammerman and Shafer, 2005; Vovk et al., 2017; Angelopoulos, Barber and Bates, 2024). Higher coverage yields longer regions, trading confidence for precision; lower coverage shortens the regions at the cost of reduced confidence.

The essential requirement for conformal prediction is that the observations used to construct the regions are exchangeable—that is, the order in which they are realized does not affect their joint distribution. Dependence among the observations is permissible so long as exchangeability holds. For example, random sampling without replacement from a finite population induces dependence but still yields exchangeable samples.<sup>7</sup>

The longitudinal data from the Longyearbyen weather station exhibit temporal dependence, precluding exchangeability. However, if residuals from a fitted model are indistinguishable from white noise, they may be treated as exchangeable and serve as valid non-conformal scores. In that case, adaptive conformal prediction regions can be computed, allowing forecast-specific intervals of varying length (Romano, Patterson and Candès, 2019). The length of each interval depends on the local uncertainty associated with the corresponding forecast.

---

<sup>7</sup>Resampling methods can address lack of exchangeability due to data dependence (Politis, Romano and Wolf, 1999, Chaps. 3–4), but such methods are beyond the scope of this paper.

Residuals from the 2023 quantile gradient-boosting fit displayed temporal dependence, so exchangeability was not initially achieved. Examination of the residual autocorrelation function suggested a simple AR(1) specification as a special case of an ARIMA model (Box et al., 2015). A single autoregressive coefficient and an intercept were estimated. When applied to the 2023 residuals, the estimated AR(1) coefficient was 0.46 and the intercept  $-1.44$ . Temporal dependence was real but modest. An autocorrelation plot of the AR(1) residuals showed no remaining dependence, and a Ljung–Box test for serial correlation produced a  $p$ -value of 0.31. The AR(1) model can therefore be regarded as part of the training algorithm that generates white-noise residuals. These residuals serve as acceptable non-conformal scores, restoring exchangeability.

The AR(1) model took the form

$$r_t = \phi_0 + \phi_1 r_{t-1} + \epsilon_t,$$

where  $t$  indexes day,  $r_t$  denotes the 2023 boosting residuals,  $\phi_0$  and  $\phi_1$  are the intercept and autoregressive coefficient, and  $\epsilon_t$  represents the ARIMA innovations. With  $\phi_1 > 0$ , the variance of  $\epsilon_t$  is smaller than that of  $r_t$ . The non-conformal scores based on  $\epsilon_t$  are therefore in the scale of the ARIMA residuals rather than the original temperature scale. Consequently, the innovations were inflated by the factor  $1/\sqrt{1 - \phi_1^2}$  to restore the appropriate scale; these inflated residuals are the final non-conformal scores.

The 2024 data served as a pristine holdout sample, representing unlabeled cases for true forecasting. Forecasts were produced using the trained quantile gradient-boosting algorithm and its `predict()` function in R, with the same predictors used earlier for fitting the 2 p.m. temperatures.

For the adaptive conformal prediction regions, a region is computed for each unlabeled case. The inflated ARIMA non-conformal scores were regressed on all predictors and the corresponding forecasts using quantile random forests (QRF) rather than quantile gradient boosting, because the latter proved numerically unstable.<sup>8</sup> For each case, the QRF output provided its  $Q(0.10)$

---

<sup>8</sup>Quantile gradient boosting (QGB) directly minimizes a global quantile loss to estimate conditional quantiles (Friedman, 2001), whereas quantile regression forests (QRF) use variance-based tree splits and recover quantiles from the empirical distribution of responses within the terminal nodes (Meinshausen, 2006). When  $\tau$  is near the extremes, sparsity can hinder QGB’s loss minimization. Because QRF computes quantiles after all trees are grown, such sparsity is avoided. Moreover, once residuals are white noise, the bootstrap sampling in QRF does not distort temporal dependence, since none remains.

and  $Q(0.90)$  values as lower and upper bounds, respectively, corresponding to a nominal coverage of at least 0.80.

Formally, with a coverage probability of 0.80,  $\alpha = 0.20$ . Let  $t = 1, \dots, T$  denote observed cases and  $T + 1$  index a new case with covariates  $\mathbf{x}_{T+1}$ . The inflated ARIMA innovations, treated as exchangeable non-conformal scores, define a distribution  $C$ . With  $y_{T+1}$  unknown, the trained boosting algorithm yields the forecast  $\hat{y}_{T+1}$  given  $\mathbf{x}_{T+1}$ . The corresponding lower and upper quantiles are

$$\hat{q}_{\alpha/2, (T+1)}(C) \quad \text{and} \quad \hat{q}_{1-\alpha/2, (T+1)}(C),$$

producing the adaptive conformal prediction region

$$[\hat{q}_{\alpha/2, (T+1)}(C) + \hat{y}_{T+1}, \hat{q}_{1-\alpha/2, (T+1)}(C) + \hat{y}_{T+1}].$$

Full pseudocode appears in the Appendix.

The lengths of the 2024 conformal prediction regions varied widely, consistent with Figure 3. Their average half-width was about  $\pm 2.5^\circ\text{C}$  for days when the forecasted temperature exceeded 0, and about  $\pm 4.5^\circ\text{C}$  when it was colder. The longest intervals reached roughly  $\pm 4.5^\circ\text{C}$  for warm days and  $\pm 8^\circ\text{C}$  for cold ones.

Interpreting these uncertainty estimates may be difficult for stakeholders. Perhaps more relevant is the likelihood that the actual future future temperature will exceed  $0^\circ\text{C}$  given a particular forecast. For forecasted temperatures above 0, these represent true positives; for forecasted temperatures at or below 0, false negatives.

Figure 7 provides a visual summary. The horizontal axis shows the mean of the daily forecasted temperatures for each of 20 equal-width bins. Because the actual temperatures are known for the 2024 holdout cases, the vertical axis shows the percentage of forecasts within each bin whose true future temperature exceeded 0. (The 14-day lag of each predictor ensures that these are future outcomes.)

The conclusions from Figure 7 are straightforward. False negatives are few—at most slightly under 20% of the forecasts in a bin—and occur mainly when the forecasted temperature lies between about  $-2^\circ\text{C}$  and  $-1^\circ\text{C}$ . When the forecasted temperature exceeds  $0^\circ\text{C}$ , more than 80% of the forecasts in a bin correspond to actual temperatures above 0, reaching 100% when the bin mean exceeds  $4^\circ\text{C}$ . The large vertical gap between filled and open circles highlights the phase transition at  $0^\circ\text{C}$ .

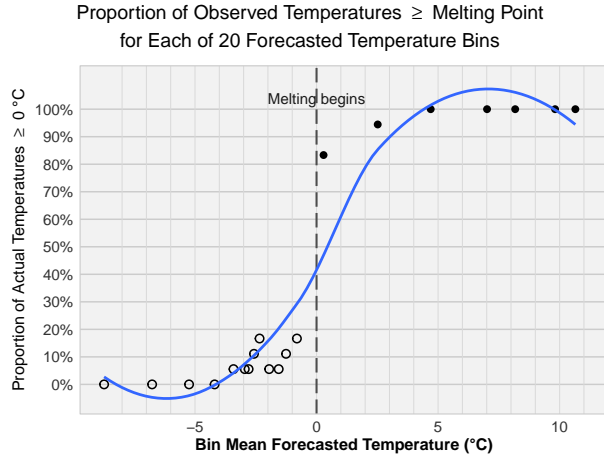


FIG 7. Mean forecasted temperature (horizontal axis) versus the percentage of cases in each of 20 equal-width bins where the true future temperature exceeded 0°C (vertical axis). Filled circles correspond to bins with mean forecasted temperature above 0°C; open circles to those below. The solid blue line is a loess smoother. Constructed from the 2024 holdout dataset.

Physical interpretation is subtle. When sea ice forms, its hexagonal lattice cannot readily incorporate salt ions. The excluded salt forms brine pockets and channels among the ice grains, leaving the ice nearly fresh water while the brine becomes increasingly saline. As freezing continues, the concentrated brine's freezing point can fall well below 0°C. Before that stage, a two-phase mixture of nearly pure ice and brine exists; melting reverses this process. Pure ice begins melting at 0°C, whereas frozen brine melts at lower temperatures.

The rates of melting and freezing depend on cloud cover, winds, and ocean currents that transport warmer or cooler water to local sites. Consequently, freezing and melting occur over a range of temperatures and time scales rather than at a fixed threshold. This interpretation aligns with Figure 7. From a policy perspective, even approximate information about when melting will occur can be valuable. Although figures like Figure 7 cannot be produced prospectively—since future temperatures are unknown—they can be constructed retrospectively using historical weather station data. Such analyses help stakeholders gauge likely rates of true positives and false negatives conditional on forecasted temperature.<sup>9</sup>

<sup>9</sup>The plotted proportions should not be interpreted as probabilities. Temporal dependence persists among the observed temperatures within each bin, though its structure is not

Given this context, the role of conformal prediction regions can be revisited. For a new, unlabeled case  $T+1$ , the true temperature will exceed the lower bound  $L_{T+1}$  of its prediction region with probability at least  $1 - (\alpha/2)$ . For  $\tau = .80$ , that probability is .90. Moreover, because the conformal prediction regions are adaptive, they provide case-specific information: as shown earlier, forecasts above  $0^\circ\text{C}$  on the average yield narrower prediction regions than those for colder conditions.

## 7. Discussion

The analysis of 2 p.m. temperatures in Svalbard, Norway, combines three statistical traditions in an unusual way: supervised learning with a quantile as the estimation target, time-series analysis making use of credible hold-out samples, and adaptive conformal prediction regions constructed with a different flavor of supervised learning.

The statistical procedures were informed by extensive knowledge of the research site. Equally important was guidance from climate science in formulating the algorithms and interpreting their output. The aim was to contribute both to scientific understanding and to climate-adaptation policy.

A two-week forecasting lead time before the onset of widespread surface melting is a very short fuse but would give Arctic community administrators critical time to prepare for infrastructure, safety, and logistical challenges (Streletsckiy, Shiklomanov and Christiansen, 2019; U.S. Arctic Research Commission, 2003). Local governments could limit heavy-vehicle use on thaw-sensitive roads, runways, and around pipelines; pre-position maintenance materials; and inspect culverts, bridges, and drainage channels before damage occurs (Arctic Research Consortium of the United States (ARCUS), 2021). Water managers could adjust reservoir levels or activate temporary treatment measures to mitigate siltation and contamination from meltwater inflows.

In communities dependent on ice roads, snowmobile trails, or frozen river crossings, early warnings would permit orderly resupply and fuel delivery before surface travel becomes unsafe (Chen et al., 2025). Coastal and hillside settlements could prepare for increased risks of shoreline erosion or permafrost-related landslides (The Climate Institute and The Firelight Group, 2022).

---

easily characterized. Observations are ordered by temperature rather than by time, and the time gaps among observations within a bin can range from days to months. For example, temperatures during late spring and early fall may be similar even though they occur several months apart.

Health authorities might use the lead time to issue advisories on water quality or vector-borne disease risk as standing water accumulates. Because of Arctic warming, Iceland is now reported to host mosquitoes (Straker, 2025).

More broadly, forecasts on a two-week timescale could foster coordination among local administrators, regional governments, and research stations, improving situational awareness and resource allocation across sectors. Even modest improvements in lead time may yield substantial adaptive benefits in Arctic regions where melt conditions evolve rapidly and logistical flexibility is limited.<sup>10</sup>

## 8. Conclusions

Projections of future global warming have long been central to IPCC assessments, complemented by many smaller-scale forecasting efforts. The analyses presented here contribute to the latter. Temperature forecasts with a two-week lead time appear promising, especially when focused on Arctic thresholds associated with widespread melting. Forecasting uncertainty is explicitly addressed, and results are presented in a manner intended to be accessible and useful to stakeholders.

The analyses also illustrate that one need not rely on “industrial-strength” data or computational infrastructure to obtain meaningful forecasts. With thoughtfully applied algorithms and accessible data, informative short-term forecasts can be generated on an ordinary desktop computer with an internet connection.

---

<sup>10</sup>The last three paragraphs were informed by a literature search undertaken by ChatGPT, which also provided initial wording later edited for consistency and style.

## Appendix

### Pseudocode 1: Constructing 2 p.m. Nonconformal Scores

**Input:** For time  $t = 1, \dots, T$ , let  $X_{t-14}$  denote the observed predictor values;  $y_t$  denote the observed 2 p.m. solar-time temperature;  $\tau$  the target quantile for the algorithmic fit; and  $\alpha$  the value determining the desired coverage probability  $1 - \alpha$ .

1. Using  $\tau$ , fit  $y_t$  with  $X_{t-14}$  via quantile gradient boosting, yielding algorithm  $\hat{Q}$ .
2. With the trained boosting algorithm  $\hat{Q}$  and  $X_{t-14}$ , compute fitted values  $\hat{y}_t = \hat{Q}(X_{t-14})$ .
3. Compute residuals  $r_t = y_t - \hat{y}_t$ .
4. If  $r_t$  shows no temporal dependence, treat  $r_t$  as exchangeable nonconformal scores.
5. If temporal dependence is present, fit a time-series procedure to  $r_t$  to obtain white-noise residuals  $\epsilon_t$ .
6. Use the white-noise residuals  $\epsilon_t$  as exchangeable nonconformal scores.
7. Using the upper and lower quantile bounds implied by  $1 - \alpha$ , fit  $\epsilon_t$  with  $y_t$  and  $X_{t-14}$  via quantile random forests  $\hat{R}$ , saving the trained algorithm  $\hat{R}$ .

**Output:** Save the nonconformal scores  $\epsilon_t$ , the trained quantile gradient-boosting algorithm  $\hat{Q}$ , and the trained quantile random-forests algorithm  $\hat{R}$  for later use with a new unlabeled case.

**Pseudocode 2: Forecasting 2 p.m. Temperatures**

**Input:** Let  $X_{T+1}$  denote the 14-day-lagged predictor values for a new unlabeled case, and let  $1 - \alpha$  be the predetermined coverage probability.

1. Use the trained quantile gradient-boosting algorithm  $\hat{Q}$  to obtain the forecast  $\hat{y}_{T+1} = \hat{Q}(X_{T+1})$  for two weeks in the future.

2. Using the trained quantile random-forests algorithm  $\hat{R}$  with predictors  $\hat{y}_{T+1}$  and  $X_{T+1}$ , obtain the conformal upper and lower bounds for case  $T + 1$ .

3. Extract from  $\hat{R}$  the fitted values  $q_{T+1,\alpha/2}$  and  $q_{T+1,1-\alpha/2}$  as the lower and upper limits, respectively, of the prediction region at coverage level  $1 - \alpha$ .

**Output:** Construct the prediction interval:

$$[\hat{y}_{T+1} + q_{T+1,\alpha/2}, \hat{y}_{T+1} + q_{T+1,1-\alpha/2}].$$

## References

ANGELOPOULOS, A. N., BARBER, R. F. and BATES, S. (2024). Theoretical Foundations of Conformal Prediction. Preprint; forthcoming with Cambridge University Press.

BALAJI, V., COURVREUX, F., DESHAYES, J., GAUTRAIS, J., HOURDIN, F. and BIO, C. (2022). Are general circulation models obsolete? *Proceedings of the National Academy of Sciences* **119** e2202075119.

BODNAR, C., BRUINSMA, W. P., LUCIC, A. et al. (2025). A Foundation Model For The Earth System. *Nature* **641** 1180–1187.

BOX, G. E. P., JENKINS, G. M., REINSEL, G. C. and LJUNG, G. M. (2015). *Time Series Analysis: Forecasting and Control*, 5 ed. Wiley, Hoboken, NJ.

BRADLEY, J. A., MOLARES MONCAYO, L., GALLO, G. et al. (2025). Svalbard Winter Warming Is Reaching Melting Point. *Nature Communications* **16** 6409.

BREIMAN, L. (2001). Statistical Modeling: The Two Cultures. *Statistical Science* **16** 199–231.

CHANG, A., LEE, H., FU, R. and TANG, Q. (2023). A seamless approach for evaluating climate models across spatial scales. *Frontiers in Earth Science* **11**.

CHEN, L. Y., MATTHEWS, N. D., JONES, B. M. et al. (2025). Increased vulnerability of Arctic potential ice roads under climate warming. *Nature*

*Communications Earth and Environment.*

U. S. ARCTIC RESEARCH COMMISSION (2003). Climate Change, Permafrost, and Impacts on Civil Infrastructure: Permafrost Task Force Report 01–03 Technical Report, U.S. Arctic Research Commission, Washington, D.C. Permafrost Task Force Report.

DANABASOGLU, G., LAMARQUE, J. F., BACMEISTER, J., BAILEY, D. A., DUVIVIER, A., EDWARDS, J., EMMONS, L. K., FASULLO, J., GARCIA, R., GETTELMAN, A. et al. (2020). The Community Earth System Model Version 2 (CESM2). *Journal of Advances in Modeling Earth Systems* **12** e2019MS001916.

NATIONAL CENTER FOR ATMOSPHERIC RESEARCH (2020). CESM2 Grid Resolution Definitions. <https://docs.cesm.ucar.edu/models/cesm2/config/grids.html>. Accessed: 2025-09-30.

NOAA NATIONAL CENTERS FOR ENVIRONMENTAL PREDICTION (2023). Global Forecast System (GFS) Model Overview. <https://www.ncei.noaa.gov/products/weather-climate-models/global-forecast>. Accessed: 2025-09-30.

EUROPEAN CENTRE FOR MEDIUM-RANGE WEATHER FORECASTS (2023). IFS Documentation: Cy47r3 - Model Resolution. <https://www.ecmwf.int/en/forecasts/documentation-and-support>. Accessed: 2025-09-30.

FRIEDMAN, J. H. (2001). Greedy Function Approximation: A Gradient Boosting Machine. *The Annals of Statistics* **29** 1189–1232.

FRIEDMAN, J. H. (2002). Stochastic Gradient Boosting. *Computational Statistics & Data Analysis* **38** 367–378.

FU, B. (2025). State of the Science Fact Sheet: Uncertainty in Forecasting Weather and Water Technical Report No. 69977, National Oceanic and Atmospheric Administration.

GETTELMAN, A. and ROOD, R. B. (2016). *Demystifying Climate Models: A User's Guide to Earth System Models*. Springer Praxis Books. Springer, Cham.

HYNDMAN, R. J. and ATHANASOPOULOS, G. (2021). *Forecasting: Principles and Practice*, 3 ed. OTexts, Melbourne.

THE CLIMATE INSTITUTE and THE FIRELIGHT GROUP (2022). The Impacts of Permafrost Thaw on Northern Indigenous Communities Technical Report, The Climate Institute and The Firelight Group.

IPCC (2019). Summary for Policymakers. In *Summary for Policymakers. In: IPCC Special Report on the Ocean and Cryosphere in a Changing Climate* (H. O. Pörtner, D. C. Roberts, V. Masson-Delmotte et al., eds.) 3–35.

Cambridge University Press, Cambridge.

KARLSEN, S. R., ELVEBAKK, A., STENDARDI, L. et al. (2024). Greening of Svalbard. *Science of The Total Environment* **945** 174130.

KEARNS, M. and ROTH, A. (2019). *The Ethical Algorithm: The Science of Socially Aware Algorithm Design*. Oxford University Press, New York.

KOENKER, R. (2005). *Quantile Regression. Econometric Society Monographs* **38**. Cambridge University Press, Cambridge, UK.

KOENKER, R. and BASSETT JR, G. (1978). Regression quantiles. *Econometrica* **46** 33–50.

KOENKER, R. and MACHADO, J. A. F. (1999). Goodness of Fit and Related Inference Processes for Quantile Regression. *Journal of the American Statistical Association* **94** 1296–1310.

KUCHIBHOTLA, A. K., KOLASSA, J. E. and KUFFNER, T. A. (2022). Post-Selection Inference. *Annual Review of Statistics and Its Application* **9** 505–527.

KVÅNUM, A. F., PALERME, C., MÜLLER, M., RABAULT, J. and HUGHES, N. (2025). Developing a deep learning forecasting system for short-term and high-resolution prediction of sea ice concentration. *The Cryosphere* **19** 4149–4166.

NOAA EARTH SYSTEM RESEARCH LABORATORY (2023). High-Resolution Rapid Refresh (HRRR) Model Description. <https://rapidrefresh.noaa.gov/hrrr/>. Accessed: 2025-09-30.

MA, Z., HUANG, J. et al. (2023). Newly reconstructed Arctic surface air temperatures since 1979 with deep learning. *Scientific Data* **10** 498.

MEINSHAUSEN, N. (2006). Quantile Regression Forests. *Journal of Machine Learning Research* **7** 983–999.

MIOSHEVICH, G., LUCENTE, D., YIOU, P. and BOUCHET, F. (2024). Extreme Heat Wave Sampling and Prediction with Analog Markov Chain and Comparisons with Deep Learning. *Environmental Data Science* **3** e9.

NISHIZAWA, S., ADACHI, S. A., KAJIKAWA, Y. et al. (2018). Decomposition of the Large-Scale Atmospheric State Driving Downscaling: A Perspective on Dynamical Downscaling for Regional Climate Study. *Progress in Earth and Planetary Science* **7**.

ARCTIC RESEARCH CONSORTIUM OF THE UNITED STATES (AR-CUS) (2021). How is permafrost degradation affecting infrastructure? <https://www.arcus.org/search-program/arctic-answers/permafrost-and-infrastructure/briefs>. Arctic Answers: Permafrost and Infrastructure Briefs.

ORTEGA, P., BLOCKLEY, E. W., KØLTZOW, M. et al. (2022). Improving Arctic Weather and Seasonal Climate Prediction: Recommendations for Future Forecast Systems Evolution from the European Project APPLICATE. *Bulletin of the American Meteorological Society* **103** E2203–E2213.

PATHAK, J., LU, Z., HUNT, B. R., GIRVAN, M. and OTT, E. (2022). Using Machine Learning to Improve Weather Forecasting. *Science* **377** 1111–1115.

PIZNER, A., POLASHENSKI, C., ROMANOVSKY, V. and STURM, M. (2024). An Examination of Water-Related Melt Processes in Arctic Snow on Tundra and Sea Ice. *Water Resources Research* **60** e2022WR033440.

POLASHENSKI, C., PEROVICH, D. K. and COURVILLE, Z. (2012). The mechanisms of sea ice melt pond formation and evolution. *Journal of Geophysical Research: Oceans* **117** C01001.

POLITIS, D. N., ROMANO, J. P. and WOLF, M. (1999). *Subsampling*. Springer, New York.

PRICE, I., SANCHEZ-GONZALEZ, A., ALET, F. et al. (2024). Probabilistic Weather Forecasting with Machine Learning. *Nature* **624** 559–563. Accessed 18 August 2025.

RANTANEN, M., KARPECHKO, A., LIPPONEN, A., NORDLING, K., HYVÄRINEN, O., RUOSTEENOJA, K., VIHMA, T. and LAAKSONEN, A. (2022). The Arctic has warmed nearly four times faster than the globe since 1979. *Communications Earth & Environment* **3**.

ROMANO, Y., PATTERSON, E. and CANDÈS, E. J. (2019). Conformalized Quantile Regression. In *Advances in Neural Information Processing Systems 32 (NeurIPS 2019)* (H. WALLACH et al., eds.) **32**.

SCHULER, T. V. et al. (2025). Svalbard's 2024 record summer: projected temperature evolution at Svalbard Airport. *Proceedings of the National Academy of Sciences* **122** e2503806122.

SEmenov, V. A. (2021). Modern Arctic Climate Research: Progress, Change of Concepts, and Urgent Problems. *Izvestiya, Atmospheric and Oceanic Physics* **57** 18–28.

STRAKER, R. (2025). Mosquitoes Have Been Found In Iceland For The First Time And Climate Change Is Blamed.

STRELETSKIY, D. A., SHIKLOMANOV, A. E. and CHRISTIANSEN, H. H. (2019). Degrading permafrost puts Arctic infrastructure at risk by mid-century. *Nature Communications* **9** 5147.

URBAŃSKI, J. A. and LITWICKA, D. (2022). The Decline of Svalbard Land-Fast Sea Ice Extent as a Result of Climate Change. *Oceanologia* **64** 535–545.

VELTHOEN, J., DOMBRY, C., CAI, J. J. and ENGELKE, S. (2023). Gradient

Boosting for Extreme Quantile Regression. *Extremes* **26** 639–667.

VOVK, V., GAMMERMAN, A. and SHAFER, G. (2005). *Algorithmic Learning in a Random World*. Springer, New York.

VOVK, V., SHEN, J., MANOKHIN, V. and XIE, M. (2017). Nonparametric Predictive Distributions Based on Conformal Prediction. *Proceedings of Machine Learning Research* **69** 82–102.